

Copyright: © 2021 by the authors. Licensee MDPI, Basel, Switzerland. This is an open access article distributed under the [Creative Commons Attribution License](#) which permits unrestricted use, distribution, and reproduction in any medium, provided the original work is properly cited.

How to Cite:

León-Cruz, J.F.; Carbajal Henken, C.; Carbajal, N.; Fischer, J. Spatio-Temporal Distribution of Deep Convection Observed along the Trans-Mexican Volcanic Belt. *Remote Sens.* 2021, *13*, 1215. <https://doi.org/10.3390/rs13061215>



Article

Spatio-Temporal Distribution of Deep Convection Observed along the Trans-Mexican Volcanic Belt

José Francisco León-Cruz ¹, Cintia Carbajal Henken ^{2,*}, Noel Carbajal ³ and Jürgen Fischer ²

¹ Departamento de Geografía Física, Instituto de Geografía, Universidad Nacional Autónoma de México (UNAM), Circuito de la Investigación Científica, Ciudad Universitaria, 04510 Coyoacán, Mexico, Mexico; jleon@igg.unam.mx

² Institute for Space Sciences, Freie Universität Berlin (FUB), Carl-Heinrich-Becker-Weg 6-10, 12165 Berlin, Germany; juergen.fischer@fu-berlin.de

³ División de Geociencias Aplicadas, Instituto Potosino de Investigación Científica y Tecnológica A.C. (IPICYT), Camino a la Presa de San José 2055, Lomas 4ta Secc, 78216 San Luis Potosí, San Luis Potosí, Mexico; noelc@ipicyt.edu.mx

* Correspondence: cintia.carbajal@wew.fu-berlin.de; Tel.: +49-30-838-56657

Abstract: Complex terrain features—in particular, environmental conditions, high population density and potential socio-economic damage—make the Trans-Mexican Volcanic Belt (TMVB) of particular interest regarding the study of deep convection and related severe weather. In this research, 10 years of Moderate-Resolution Imaging Spectroradiometer (MODIS) cloud observations are combined with Climate Hazards Group Infrared Precipitation with Station (CHIRPS) rainfall data to characterize the spatio-temporal distribution of deep convective clouds (DCCs) and their relationship to extreme precipitation. From monthly distributions, wet and dry phases are identified for cloud fraction, deep convective cloud frequency and convective precipitation. For both DCC and extreme precipitation events, the highest frequencies align just over the higher elevations of the TMVB. A clear relationship between DCCs and terrain features, indicating the important role of orography in the development of convective systems, is noticed. For three sub-regions, the observed distributions of deep convective cloud and extreme precipitation events are assessed in more detail. Each sub-region exhibits different local conditions, including terrain features, and are known to be influenced differently by emerging moisture fluxes from the Gulf of Mexico and the Pacific Ocean. The observed distinct spatio-temporal variabilities provide the first insights into the physical processes that control the convective development in the study area. A signal of the midsummer drought in Mexico (i.e., “canícula”) is recognized using MODIS monthly mean cloud observations.

Keywords: deep convection; associated severe weather; precipitation; complex terrain; MODIS; CHIRPS



Citation: León-Cruz, J.F.; Carbajal Henken, C.; Carbajal, N.; Fischer, J. Spatio-Temporal Distribution of Deep Convection Observed along the Trans-Mexican Volcanic Belt. *Remote Sens.* **2021**, *13*, 1215. <http://doi.org/10.3390/rs13061215>

Academic Editors: Vinay Kumar and Ismail Gultepe

Received: 3 February 2021

Accepted: 19 March 2021

Published: 23 March 2021

Publisher's Note: MDPI stays neutral with regard to jurisdictional claims in published maps and institutional affiliations.



Copyright: © 2021 by the authors. Licensee MDPI, Basel, Switzerland. This article is an open access article distributed under the terms and conditions of the Creative Commons Attribution (CC BY) license (<https://creativecommons.org/licenses/by/4.0/>).

1. Introduction

Clouds play a key role in global climate regulation. Their interaction with large-scale atmospheric circulations primarily results from three processes: phase changes, radiative transfer and the turbulent transport of air parcels [1]. The study of these cloud feedbacks is essential to gain a better understanding of the association between atmospheric circulations and the cloudiness that characterizes the weather regimes [2]. It is also necessary for the correct parameterization of clouds in general circulation models (GCMs) [3–5].

Within the extensive diversity of clouds, those associated with strong vertical growth (i.e., towering cumulus/cumulonimbus) are of particular interest. In addition to their impact on atmospheric dynamic and thermodynamic processes, even towards climate scales (e.g., [6]), they may also affect their local environment in a socio-economic way. These kinds of deep convective clouds (DCCs) can develop into severe storms with associated severe weather patterns such as lightning, large hail, heavy rainfall leading to flash flooding,

strong winds and even tornadoes, which in turn may have significant socio-economic impacts; for example, in the aviation industry (icing, downbursts) the agricultural sector (bad crops) and the insurance industry (damage due to storms).

In this sense, Hoeppe [7] reports, for the period 1980–2014, that 41% of loss events, property damage and bodily injuries worldwide are related to meteorological causes (including convective and local storms). These kinds of events also represent 25% of fatalities and 71% of insured losses. Weather-related disasters around the globe also show a positive trend in occurrence and damage [7]. In Europe, a similar trend for tornadoes, violent winds, flash floods and large hail is observed [8]. Likewise, in Mexico and Central America, weather-related disasters represent the largest percentage of the total societal impacts associated with natural hazards [9].

The link between severe storms, associated severe weather and deep moist convection is well known, though the accurate nowcasting remains a substantial challenge [10–12]. There are many parameters and complex processes at different spatial and temporal scales involved in the generation of severe weather. At the local level, the boundary layer processes, the terrain, and surface effects such as baroclinic vorticity or mountain-valley circulations are present. Furthermore, advective processes such as differential advection, convergence lines and moisture advection must be considered [13,14]. Finally, there are dynamical processes such as mesoscale instabilities and gravity waves [13]. Besides the study of processes leading to severe weather, another way to improve our understanding of these events is the characterization of the environmental conditions in which these systems form, as well as the observation and quantification of the spatio-temporal distributions of severe weather systems themselves.

The detection and monitoring of deep convection and associated severe weather and the characterization of the environments in which they form are based on different perspectives. The ingredients-based approach [15] with reanalysis data, in which relationships are based on parameters as the convective available potential energy (CAPE) and deep-layer shear for the determination of severe weather environments, is one of the most employed methods. For example, in Brooks et al. [16] reanalysis data are used to estimate the frequency of favorable conditions to compute the spatial distribution of severe thunderstorm and tornado environments on a global scale. Furthermore, soundings and ground-based observations are widely used to forecast, detect and monitor deep, moist convection and associated severe weather. For example, in Taszarek et al. [17], a large set of sounding measurements is combined with ERA-Interim reanalysis to assess the spatial and temporal distributions of the prerequisites of deep, moist convection across Europe. In Matsudo and Salio [18], data from a surface station network are used to document the occurrence and spatial distribution of severe weather phenomena associated with deep, moist convection over southeastern South America. In Goudenhoofd and Delobbe [19] reflectivity measurements from C-band weather radar are used to study the characteristics of convective storms in Belgium, such as the probability of occurrence of a storm and its correlation with orographic variations. In addition to using model, sounding and ground-based data, several studies regarding severe weather research focus on the use of satellite observations. One of the main advantages of satellite data is the large-scale spatial coverage as well as high temporal coverage, depending on the type of satellite and on-board instruments.

In countries like Mexico, where, due to the lack of ground-based instruments such as weather radars for many regions, no wide-scale severe weather detection and monitoring exists, the use of satellite data turns into an affordable alternative. A broad spectrum of measurements from several passive and active instruments mounted on different types of satellites and the large set of atmospheric parameters that can be subsequently inferred is available. For example, Devasthale and Fueglistaler [20] analyzes, from a climatic perspective, the spatial distribution of deep convection over India using measurements from the Advanced Very-High Resolution Radiometer (AVHRR) and cloud datasets obtained from the Moderate-Resolution Imaging Spectroradiometer (MODIS) mounted on various

polar-orbiting satellites. Matsudo and Salio [18] explores the relationship of severe weather documented with the surface station network to mesoscale convective systems (MCS) observed with measurements from the Geostationary Operational Environmental Satellite-12 Infrared (GOES-IR). Takahashi and Luo [21] utilizes a joint analysis of cloud profiling radar (CPR) observations from CloudSat and geostationary satellite data to characterize tropical deep convective clouds. In Carbajal Henken et al. [22], a combination of radar measurements and a set of cloud physical properties retrieved from measurements from the Spinning Enhanced Visible and Infrared Imager (SEVIRI) on the Meteosat Second Generation (MSG) geostationary satellites is exploited to investigate the possibility of automatic detection of deep convective clouds in the Netherlands. Rosenfeld et al. [23] presents a conceptual model for the detection of severe convective storms, producing tornadoes and large hail, based on satellite-retrieved vertical profiles of cloud top temperature and particle effective radius relations from AHVRR data and geostationary satellites. Although many other studies are dedicated to this type of research, those mentioned above give an idea of the multiple applications that satellite data can have for the study of deep convection-associated severe weather and the environments in which it forms.

In Mexico, there is little documentation of severe convective storms and their multiple manifestations. Recently, Valdés-Manzanilla [24] explored several characteristics of MCSs, and Zúñiga and Magaña [25] analyzed extreme precipitation events. Some characteristics of the convective storms and their relationship to the cloud-to-ground lightning have been studied as well [26,27]. Moreover, supercell storms and tornadoes in the northeastern part of Mexico have been studied [28,29]. Given that tornadoes are one of the most violent manifestations of severe weather, they can be used to delimit the areas where extreme meteorological events occur. In this sense, the TMVB stands out as a region of great importance. Previous studies highlight the influence of the environmental and topographic characteristics of the TMVB in the generation of non-supercell tornadogenesis [30]. This area in central Mexico experiences about 40% of total tornadic activity recorded in the country [31,32] (Figure 1a).

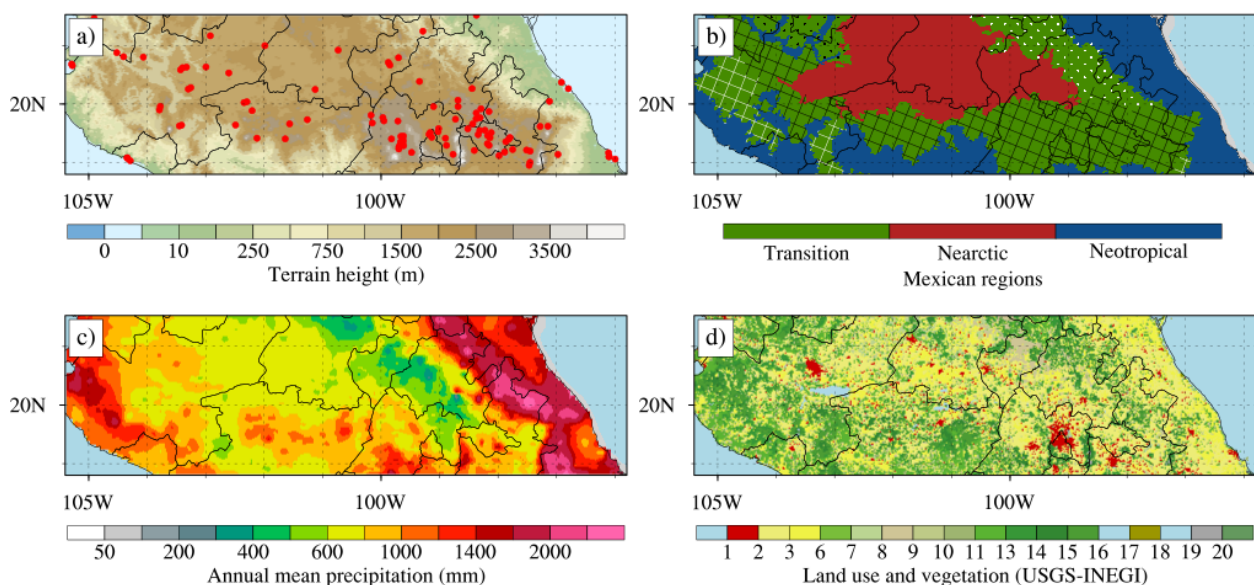


Figure 1. Distribution of (a) terrain elevation, (b) Mexican regions [33], (c) annual mean precipitation rate (mm) (2008–2017) and (d) land-use and vegetation (see Table in Appendix A) over the study area. In (b), the sub-areas of the transition zone, Trans-Mexican Volcanic Belt (TMVB), Southern Sierra Madre (SSM), Eastern Sierra Madre (ESM) and Western Sierra Madre (WSM) are indicated with the following fill patterns: black squares, white squares, white dots and black dots, respectively. In (a), the red points indicate the locations of reported tornadoes (2008–2017) [32].

In this context, this research aims to exploit a combination of independent, well-established satellite-based observational datasets with large coverage to assess the fre-

quency occurrence and natural variability of DCCs in the TMVB region. Thus, 10 years of MODIS Collection-6 cloud data are combined with the Climate Hazards Group Infrared Precipitation with Station (CHIRPS) data. The substantial sampling of the satellite observations provides the opportunity for the first estimation of the spatio-temporal distributions of deep convective cloud systems and associated severe weather in the form of extreme precipitation. For future model-based studies, the observed spatio-temporal characteristics can provide valuable information about the quality of physical parameterizations, which would be relevant for convective cloud development and associated severe weather.

The paper is organized as follows. Section 2 introduces the study area, while Section 3 describes the datasets and methods used. Section 4 presents the results and corresponding discussions. First, the MODIS-based spatio-temporal distributions of cloud fraction and deep convective clouds in the study area are characterized. Then, spatio-temporal relationships between observations of deep convection and extreme precipitation events, as well as the relation to geographical variations in the form of terrain height, are assessed. Then, a sub-region analysis allows a first examination of the possible influence of varying local and large-scale conditions and accompanying physical processes on the satellite-observed deep convection distributions. Finally, conclusions are given.

2. Study Area

The region selected for this study is located over the central part of Mexico, from 18.8°N, 105.4°W to 21.5°N, 95.7°W, with an area coverage of ~324,483 km². The criteria for this selection were based on the significant number of tornado reports in the area (taken as a trace of severe weather), the prevalent complex terrain (serving as a static parameter in the generation of deep convection) and the large population exposed to these natural phenomena (considered as one of the risk components). Due to the amount of recently documented tornadic activity in this part of the country (Figure 1a), it is also known as the Mexican Tornado Alley (MTA). Given that these tornado climatologies are based on documentary information (i.e., social networks, eyewitnesses, newspapers and official information from authorities), it is evident that the total number of tornadoes in Mexico is underestimated [32].

The study area extends along the influence zone of the TMVB. The TMVB has a complex orography with elevations between 0–5000 m above sea level; see Figure 1a. It is defined as a transition zone among the Nearctic and the Neotropical regions [33], separating drier climates to the north from the humid ones to the south; see Figure 1b. Likewise, the mountain ranges of the TMVB represent a great natural barrier in the propagation of cold fronts from the north and moisture fluxes from the Pacific Ocean and the Gulf of Mexico [31].

Due to its geographical position between the Pacific Ocean and the Gulf of Mexico, the study area is influenced by tropical cyclones, cold fronts and easterly waves. These weather systems have a significant impact on the natural characteristics of this zone; see Figure 1d. For example, the center-north region is dominated by drylands, pastures and shrublands (in yellow tones), associated with the drier portion of the domain. In contrast, the center-south shows abundant vegetation with evergreen and deciduous forests (in green tones). In the eastern part, the coastal plain of the Gulf of Mexico, irrigated and dryland croplands dominate, while at the highest elevations, woodlands dominate. The western sub-region is dominated by cropland/woodland. It is important to mention that two of the most populated cities in Mexico, Mexico City and Guadalajara, are located in the study area (in red tones).

The mean annual precipitation rate over the study area, computed for the years 2008–2017, shows the greatest values (near the 3000 mm/year) in the east sub-region; see Figure 1c. In general, high precipitation amounts are aligned with higher terrain elevations; i.e., the contribution of convective precipitation is high, at least in this part of Mexico. Along the TMVB, values between 600–1200 mm/year are shown. The area at the west of the Eastern Sierra Madre mountain range displays the minimum values

(~300 mm/year), coinciding with an area affected by the Föhn effect and the dryer portion of the domain [34]. In summary, the relationship between precipitation–terrain–land-use and vegetation is clear.

3. Material and Methods

3.1. MODIS Data

MODIS is a passive imager mounted on both the Terra and Aqua sun-synchronous polar-orbiting satellites, with equator crossings for the descending and ascending nodes at approximately 10:30 A.M. and 1:30 P.M. local time, respectively. It is a 36-channel whiskbroom scanning radiometer measuring between 0.405 and 14.385 μm . It has a viewing swath width of 2330 km and nadir spatial resolutions of 250 m, 500 m and 1000 m, depending on the channel. A large number of data products from MODIS observations are useful to describe features of the land, the oceans and the atmosphere. MODIS observations can be used, for example, in studies of geophysical processes and phenomena from local to global scales. MODIS atmosphere products are archived into two categories: pixel-level retrievals (Level-2) and global gridded statistics (Level-3).

In this study, Collection 6 (C6) of the cloud optical and micro-physical data at a 1 km resolution as well as macro-physical products at a 5 km resolution from Level-2 MODIS data were collected [35]. The C6 algorithm contains several changes and improvements compared with C5, as described in Platnick et al. [36]. In the Level-2 products, the MODIS cloud mask was used to discriminate clear-sky pixels from clouds. In the next step, the cloud optical and micro-physical properties were retrieved for cloudy pixels. Additionally, cloud properties derived from thermal infrared bands were obtained [37]. MODIS data were stored in Hierarchical Data Format (HDF) and divided into MOD06_L2 (collected from the Terra platform) and MYD06_L2 (collected from the Aqua platform). Ten years (2008–2017) of different parameters, such as cloud top pressure (CTP), cloud optical thickness (COT) and cloud fraction (CF), were collected for the study area. The temporal coverage of MODIS observations from Aqua and Terra was from 16:00 GMT to 22:00 GMT (11:00 to 17:00 local time) in the study area.

3.2. Definition of Deep Convective Cloud

There are several established ways to detect and characterize deep convection from satellite-based passive imagery. In general terms, deep convective clouds have pronounced vertical growth, leading to low observed brightness temperatures and thus to retrievals of low values of cloud top temperature (CTT) and cloud top pressure (CTP). They also have high liquid/ice contents that produce high reflectances in the solar part of the spectrum, which leads to, e.g., retrievals of high cloud optical thicknesses (COTs). Cloud classification schemes based on joint histograms of two or more cloud parameters retrieved from passive observations have been widely used in the satellite research community. For example, in King et al. [5], a combination of cloud top properties, optical and micro-physical properties were used to describe MODIS-observed spatial and temporal distributions of cloud regimes on a global scale; among others, those associated with deep convective activity. Threshold values of MODIS-based cloud brightness temperature (BT) and COT have been used for the detection and DCC property description over different locations of the globe by Yuan and Li [38], while Jin et al. [39] used a combination of MODIS-based CTP and COT to describe large-scale characteristics of tropical convective systems. Similar parameters were used by Ntwali and Chen [40] to estimate the probability of deep convection in Africa.

For this study, we used a straightforward cloud type definition of deep convective cloud taken from the well-established International Satellite Cloud Climatology Project (ISCCP) [41,42]. For many years, in a time period starting in the early 1980s until 2015, ISCCP has been providing a large set of gridded atmospheric products with temporal resolutions ranging from 3 h to monthly means and spatial resolutions ranging from 2.5 degrees up to 10 km in more recent efforts. The cloud climatologies are based on a combination of measurements from geostationary satellites and AVHRR instruments

mounted on several National Oceanic and Atmospheric Administration (NOAA) polar-orbiting satellites. Specifically, a satellite pixel covers a deep convective cloud when the retrieved CTP is equal or less than 440 hPa and the retrieved COT is equal or greater than 23.

Here, we took advantage of the advanced MODIS cloud retrievals, higher pixel resolution and large sampling. The MODIS-based deep convective cloud observations were collected for a grid with resolution 0.1° , which allowed the analysis of deep convection frequencies and their relationship with local characteristics such as the topography. The DCC frequency per grid cell was obtained from average CTP and COT values, which were computed from the collected MODIS cloudy pixels that fell within the grid cell for each daytime satellite overpass. Note that only cloudy pixels with successful CTP and COT retrievals were used (and that the cloud phase was not explicitly taken into account). To count a MODIS-observed DCC event, both CTP and COT average values needed to fulfill the threshold requirements mentioned above. The monthly values of the total number of observed DCCs, or DCC frequencies, were obtained by adding daily DCC counts.

A CTP of 440 hPa relates to a height of about 6.5 km. In the study area, parts of the Transition and Nearctic sub-regions consist of high plains (altiplano) with an elevation height of about 2 km. In addition to a horizontal extent of at least about $10 \text{ km} \times 10 \text{ km}$, meaning that single clouds at the very beginning of convective development are not considered, the clouds can still have a considerable vertical extent, also at higher elevations. Moreover, the combination with the COT threshold ensured that only clouds with a high liquid/ice content, which depends on thermodynamic variables, were included. In that sense, COT can be considered as additional information on cloud vertical development, noting that the retrieval of COT is largely independent of cloud top height.

Although the temporal coverage of the daytime MODIS observations ranges from 16:00–22:00 GMT, it allows the characterization of developing convective cloud systems, including (part of) their mature stage. Taking into account the fact that in the process of convection initiation, the daytime heating has a significant influence [43], the MODIS cloud observations within these 6 h serve as a good indicator of the general conditions that determine the generation and frequency of deep convective cloud systems in this part of Mexico.

3.3. CHIRPS Data

The CHIRPS is a 30+ year quasi-global rainfall dataset. It spans from 50°S – 50°N with a high spatial resolution of 0.05° . CHIRPS data contain information only from continental areas and at multiple temporal resolutions. This dataset includes three principal components: global climatologies, satellite measurements (at infrared wavelengths) and in-situ observations [44]. Among the advantages of CHIRPS are their great geographical coverage, temporal uniformity, their validation processes and the quasi-real-time updates. Several studies have been conducted worldwide to validate this dataset [45–47]. Mexico is one of the principal collaborators in in-situ observations of CHIRPS [44], and recently, different investigations have been realized in the country using this dataset [48,49]. For example, in 2017, an average of 335 meteorological stations per month were used in the CHIRPS dataset, only for the area of the TMVB. In this study, the 2.0 version of the CHIRPS dataset was used to assess the spatio-temporal distribution of precipitation and extreme events in the TMVB. Daily data [50] from 2008–2017 with a spatial resolution of 0.05° were processed. Although the CHIRPS dataset used includes the entire diurnal cycle, the significant contribution of the afternoon and early night precipitation in the study zone just before or even through the last MODIS observations [51,52] helped us to understand the contribution of these convective clouds to the precipitation regime.

4. Results and Discussion

4.1. Spatio-Temporal Distribution of Cloud Fraction

In the first step, the observed spatial and temporal distribution of cloud fraction is presented in Figure 2. The CF distribution represents the average of 10 years by grid point, where 1 means a zone completely covered by clouds and 0 represents a cloud-free region. In this analysis, high, middle or low clouds are not differentiated. The primary purpose is to establish the first impression on the cloudy situation in the region and relate these spatio-temporal distributions of clouds to dry and wet seasons. Such a behavior can be a result of the interaction of local static conditions (such as terrain features) and dynamic parameters (such as moisture fluxes, frontal activity, mesoscale systems or even climatic oscillations). From the analysis of the CF monthly climatologies, two principal phases have been identified. First, there is a wet season, from June–September, which mostly includes the summer months. The highest values of CF correspond to topographic features such as mountain ranges in the TMVB, Eastern and Western Sierra Madre and the coastal plains of the Gulf of Mexico and the Pacific Ocean. The other factor relating to this distribution is the sea breeze effect in coastal areas [52]. The impact of this type of circulation, for example, on cloud development, fog production and storm initialization, has been well-documented [53]. Second, the months from November to April are characterized by a constant decrease in CF values across the domain. CF values less than 0.3 are typical in most parts of the territory, except in the Gulf of Mexico. From November to February, these high values of CF are associated with the passage of cold winter fronts in this region of Mexico [54]. March and April are the drier months in this phase. Lastly, two smaller transition phases can be identified: first, in May as a dry transition; and second, in October as a wet transition. Maximum values of CF are located over the east during the May transition, while during the October transition, the maximum CF values are located over the central and the western portions of the domain. Such a situation suggests a transition from east to west as discussed above.

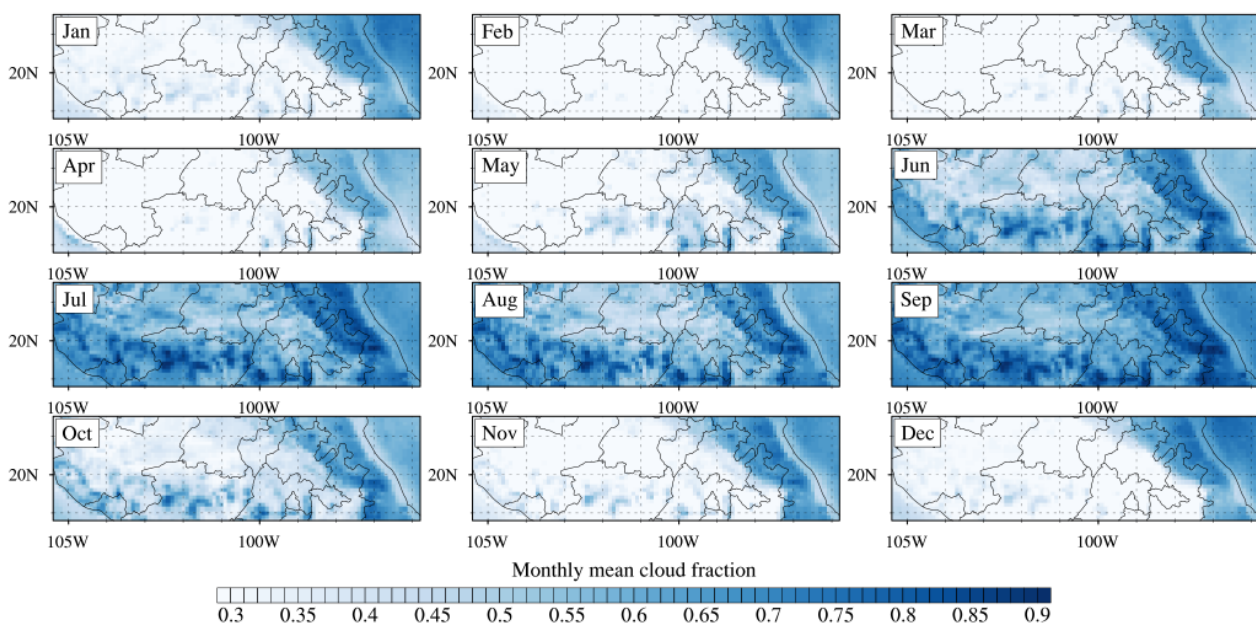


Figure 2. Monthly distribution of mean cloud fraction based on Moderate-Resolution Imaging Spectroradiometer (MODIS) cloud data (2008–2017) with a horizontal resolution of 0.1 degrees.

4.2. Spatio-Temporal Distribution of Deep Convective Clouds and Severe Weather Events

The monthly distribution of observed DCC frequencies on a grid with a spatial resolution of 0.1 degrees in the study area is presented in Figure 3. Note, the numbers are considered to represent single convective events for each grid box. As for the cloud

fraction, wet, dry and transition phases are noticed. In the first two winter months, the higher frequencies are located over the Gulf of Mexico and can be related to the passage of mid-latitude frontal systems enhanced by orographic effects [55], which may also consist of high COTs and low CTPs. In the next two months, in the dry season, not more than 30 DCCs are observed. May is the first transition phase, and it is when the terrain features start to play a significant role in the increase of observed DCC frequency. Between June and September, the wet phase is established. In this period, the highest observed DCC frequencies are extended along the mountains of the TMVB. Some portions of the domain show total values of over 100 DCC events per month; i.e., about 10 events per month on average or one-third of total days with convective activity. The spatial distribution of observed DCC frequency, especially in this active phase, is consistent with the spatial distribution of cloud-to-ground lightning activity described by Kucieńska et al. [26], mainly in the western part of the domain. In this wet season, the interaction of the moisture fluxes from the Gulf of Mexico and then from the Pacific Ocean (in late summer) with the terrain features seems to modulate the deep convection activity. The spatio-temporal behavior of the convection shown here shares some main characteristics with the results of Cavazos and Hastenrath [56] who described the convection and rainfall in Mexico and their relationship with the Southern Oscillation using highly reflective cloud data, upper air soundings and surface ship observations; for example, the peak activity in September along the east coast of the domain and the highest DCC frequency in the summer months in central Mexico. Another remarkable aspect is the spatial transition from east to west of the observed DCC frequency; possible reasons for this are discussed later. October is identified as a second transition phase. Although the observed DCC frequencies are low, the most active zone is over the western portion of the TMVB. The last months, November and December, follow the same pattern as January and February, but with a general decrease, even in the Gulf of Mexico. A possible explanation comes from the change of atmospheric circulation patterns and moisture availability. At this stage, dry and cold air masses from the north begin to have some influence on the study area [56,57]. These air masses work as convective inhibition elements, mainly in the northern portion of the complex terrain of the TMVB.

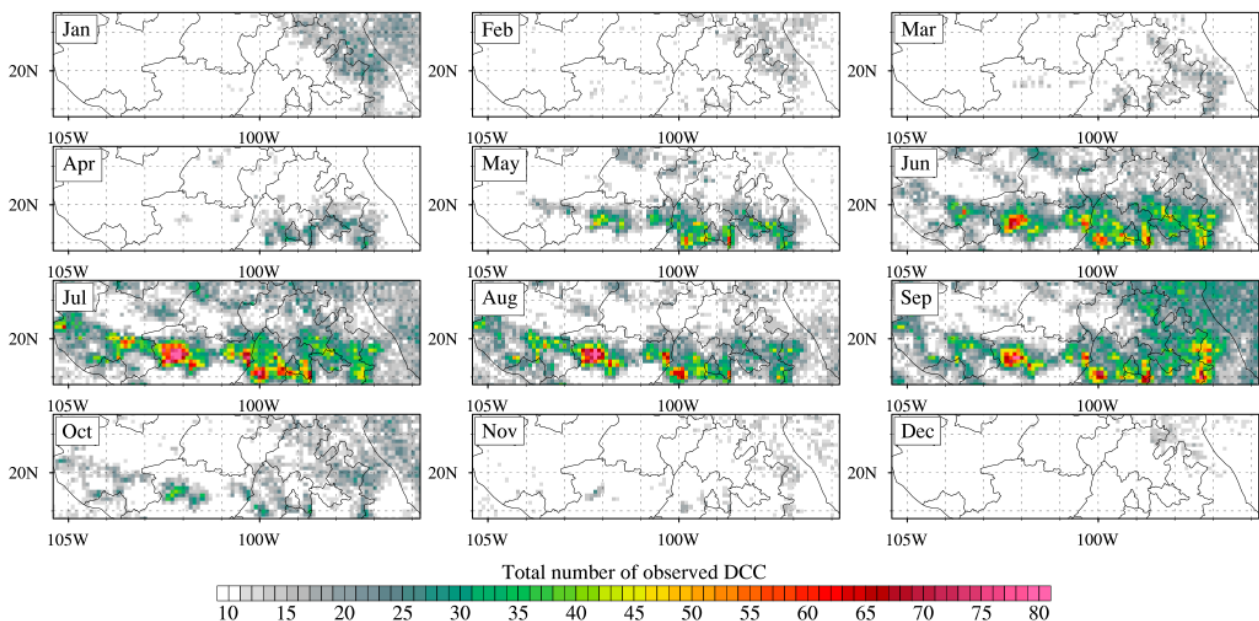


Figure 3. Monthly distribution of the total number of observed deep convective clouds based on MODIS cloud data (2008–2017) with a horizontal resolution of 0.1 degrees.

To assess the spatio-temporal relationships between the observed DCC frequency and extreme precipitation events, the monthly distribution of the number of days with daily

precipitation exceeding 10 mm (Figure 4) and the monthly distribution of precipitation threshold for the 90th percentile (Figure 5) were computed using the CHIRPS dataset. The 10 mm threshold of daily precipitation represents heavy precipitation days and is useful to identify the regions in which these events are common (adopted from the European Climate Assessment (ECA) indices of extremes). On the other hand, the 90th percentile helps to characterize the behavior of the extreme precipitation events within the study area. The similarity between the spatial-temporal distributions of heavy precipitation days (from CHIRPS, Figure 4) and convective frequency (from MODIS, Figure 3) is evident. Between June and September, the wet phase is identified, with the higher values (i.e., the most days) also located over the higher elevations. The mountainous areas at the west of the Gulf of Mexico, the central part of the TMVB and the Pacific Ocean hold the highest values, with a maximum of 175 heavy rainy days in August. Taking into account the fact that the total number of days analyzed is 3653 for 10 years, the wet areas have about a 5% occurrence (using all the days available). Concerning the precipitation thresholds obtained from the 90th percentile (Figure 5) the Gulf of Mexico stands out with more than 75 mm of daily precipitation in the summertime. The average of the wet phase (June to September) ranges higher than 40 mm/day over the regions identified with more intense rainfall activity. Again, higher values are associated with higher elevations, but in this case, the area of the Gulf of Mexico is dominant. This situation can be associated with moisture fluxes and their interaction with the local topography, as suggested by Giovannettone and Barros [58], and the possible contribution of the sea breeze. For the area of the central part of the TMVB, the threshold values range between 20–25 mm/day. One of the most important findings here is the exceptional variety of the behavior of the extreme precipitation events in a relatively small geographical area. Whereas the precipitation thresholds in the mountains near the Gulf of Mexico reach 50 mm/day or more, just a few kilometers to the west, the thresholds decrease to values close to 10 mm/day, indicating the great importance of local conditions.

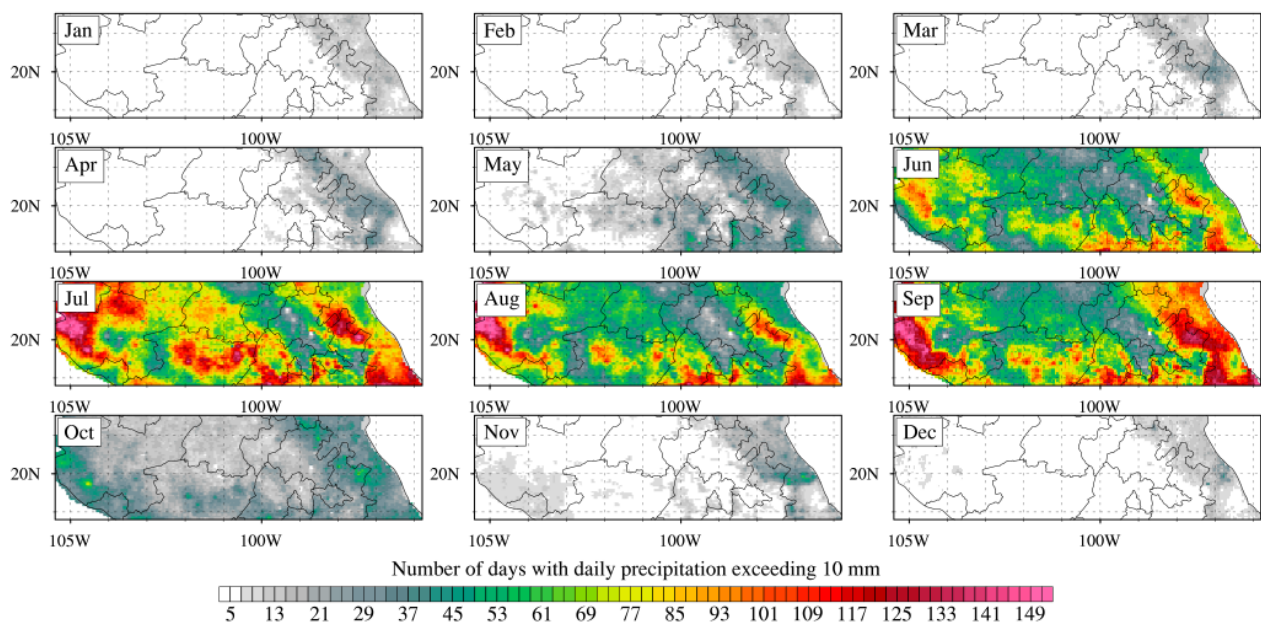


Figure 4. Monthly distribution of the total number of days with daily precipitation exceeding 10 mm based on Climate Hazards Group Infrared Precipitation with Station (CHIRPS) data (2008–2017) with a horizontal resolution of 0.05 degrees.

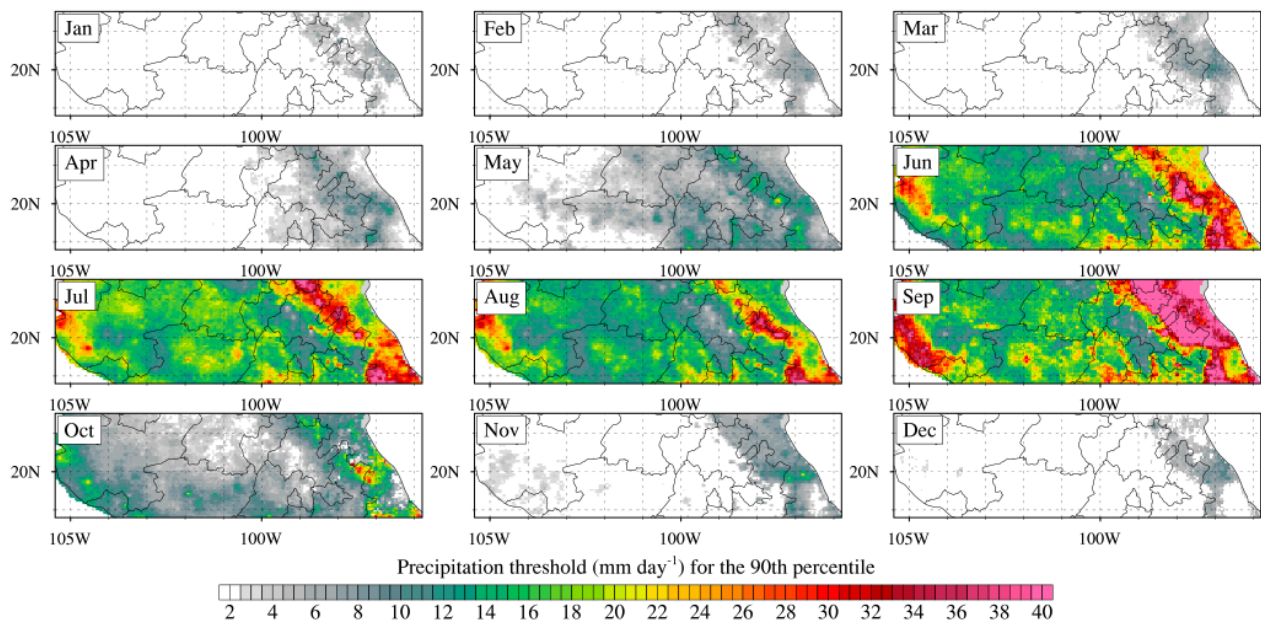


Figure 5. Monthly distribution of precipitation thresholds (mm/day) for the 90th percentile based on CHIRPS data (2008–2017) with a horizontal resolution of 0.05 degrees.

In Figure 6 the time series of the tropical cyclone activity, the total observed DCC and precipitation rates over the study area are shown. For the deep convective clouds and precipitation, the active season starts in June, with the first peak in July. Then, in August, the frequency of these two parameters has a relative minimum. The second observed peak in precipitation and deep convection activity in September indicates the influence of the passage of tropical cyclones over the study area. This time series was assessed using the analysis of the International Best Track Archive for Climate Stewardship dataset [59]. To this end, tropical cyclone tracks (2008–2017) that affected the study zone were extracted. Only systems classified as tropical depressions, tropical storms and hurricanes of categories 1–5 were used in this analysis. The results show that the maximum tropical-cyclone activity is in September, which is consistent with Jáuregui [60]. Such results relate well to the observed behavior of precipitation and deep convective cloud frequencies in the second part of the active phase. The rest of the months are identified as the transition phase (April–May and October–November), and the passive phase (December–March). Taking into account all monthly means of DCC frequency and accumulated precipitation (i.e., 120-time steps), the domain-averaged temporal correlation coefficient is 0.84, which demonstrates the strong correlation between the two observational datasets. Per season, correlation coefficients are found to be 0.79, 0.77, 0.81 and 0.93 for December–February, March–May, June–August and September–November, respectively. The variation indicates the impact of seasonal changes in weather patterns and associated phenomena (e.g., tropical cyclones, easterly waves and cold fronts) affecting the study area on the relationship between the MODIS-based DCC frequencies and CHIRPS observed precipitation.

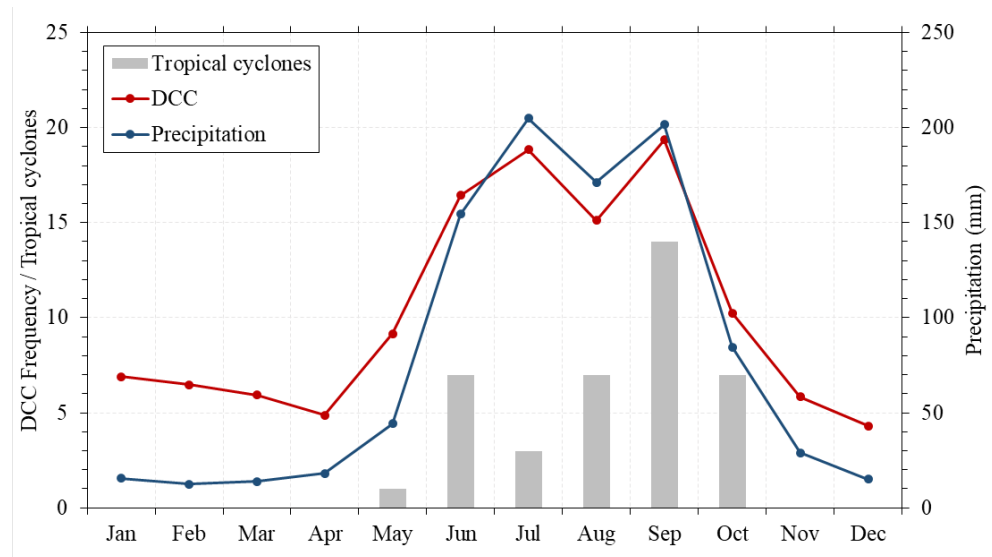


Figure 6. Monthly domain-average of deep convective cloud frequency, accumulated precipitation and tropical cyclone activity. The red line represents the domain-averaged total number of observed DCC based on MODIS data with a horizontal resolution of 0.1 degrees; the blue line represents the domain-averaged monthly mean precipitation amounts based on CHIRPS data with a spatial resolution of 0.05 degrees, and the grey bars represent the number of tropical cyclones that affected the study region. All parameters are shown for the period 2008–2017.

4.3. Relation to Terrain Height

Another feature connected to the observed DCC frequency in the study area is the terrain height. As previously mentioned, the TMVB holds a complex topography that seems to favor the development of deep convection. In this sense, the correlation value between terrain height and DCC frequency over the entire domain is 0.32. This correlation value takes into account all the grid points in inland Mexico. By dividing the domain into sub-regions (see Figure 1b), the correlation values change to 0.54, 0.57 and -0.19 for the Transition, Nearctic and Neotropical sub-regions, respectively. The relatively high correlation value in the Nearctic sub-region is associated with the comparably low terrain height variations and the subsequent low DCC frequency. A similar case is the Transition sub-region, where high terrain height variations relate to the high DCC frequency.

In order to analyze in more detail how the variations in terrain features relate to observed DCC frequencies, cross-sections at constant latitudes (20.5°N , 19.5°N , and 19.0°N) of the total number of observed DCC events and the total number of observed DCC events limited to the corresponding wet phase (June to September) are shown in Figure 7.

For the cross-section at the constant latitude of 20.5 degrees north (northern part of the domain), the observed DCC frequency shows the Gulf of Mexico as the most active region. The western part also shows relatively high frequencies. As expected, this cross-section shows a relatively stable behavior since the transect includes the dry highlands of the domain and fewer terrain height differences. The correlation coefficients for this section are -0.67 for the full period and -0.45 for the wet phase. In the second cross-section, at the constant latitude of 19.5 degrees north, which is just over the TMVB, the influence of the Pacific Ocean is evident in the western part of the domain, with peaks of frequency just over the windward side. The altitude differences mark, in this plot, the higher frequencies of the observed DCC. The correlation values for this transect are 0.63 for the full period and 0.53 for the wet phase. Finally, in Figure 7c at the constant latitude of 19.0 degrees north, including the southern portion of the TMVB and highest elevations, the correlation values increase to 0.77 for the full period and 0.76 for the wet phase. The increase in the frequency of the DCC observed in the eastern part of the domain indicate the significant role that the fluxes from the Gulf of Mexico and mountainous areas play in the generation of deep convective clouds. The relatively high correlation coefficient between observed

deep convective clouds and terrain height is a strong indicator of the considerable role of complex topographic features in the forced convection processes within the TMVB region. For spatial distribution maps of seasonal correlation values between MODIS-based frequencies of DCC and CHIRPS accumulated precipitation, we refer to the Figure S1 of the Supplementary Material.

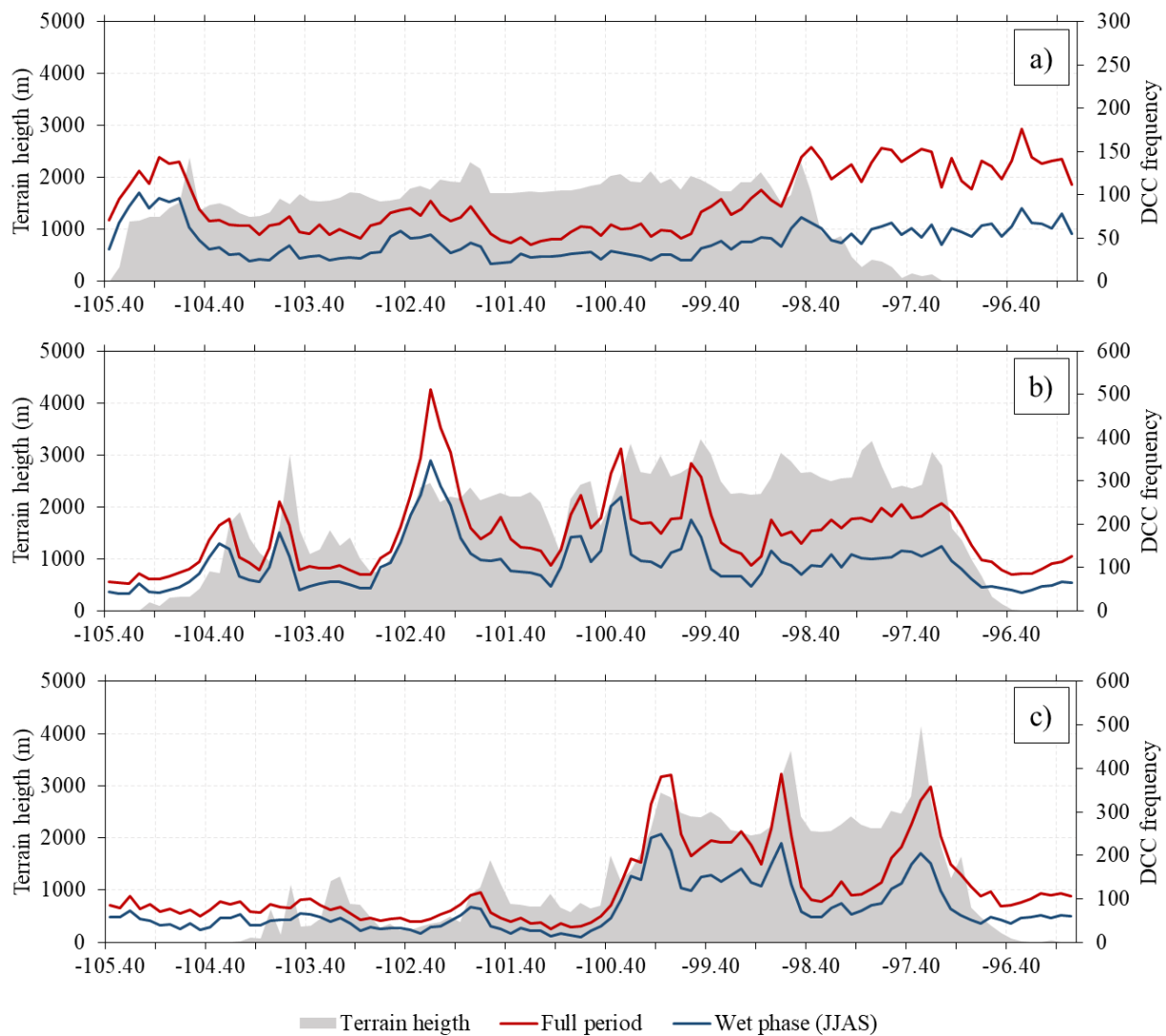


Figure 7. Cross-section at constant latitudes (a) 20.5, (b) 19.5, and (c) 19.0 degrees north of deep convective cloud frequency. The red line represents the total number of observed DCCs (2008–2017) and the blue line the corresponding values for the wet phase only (June, July, August, and September) based on MODIS data with a horizontal resolution of 0.1 degrees. The grey area shows the terrain height in meters.

4.4. Sub-Region Analysis

The study area has been divided into three sub-regions (see Figure 1b). The Neotropical region includes the coastal plains of the Pacific Ocean and the Gulf of Mexico. The lowlands of the Balsas Basin are considered to be part of this sub-region as well. This sub-region is under the immediate influence of moisture fluxes from the oceans [30]. The Nearctic region is dominated by high and drylands affected by frontal systems from the north [61]. This sub-region covers the southern portion of the Chihuahua Desert. On the other hand, the Transition region holds the main topographic features from the TMVB, the Western Sierra Madre, the Eastern Sierra Madre and the Southern Sierra Madre. This sub-region is influenced by moisture fluxes from both the Pacific Ocean and the Gulf of

Mexico. Furthermore, the position of these terrain features represents a natural barrier perpendicular to the coastal lines [31]. The geographical location of each area represents unique land surface, meteorological and climatic characteristics.

Monthly means of observed DCC frequencies and CF for each sub-region are shown in Figure 8. The values shown here represent a sub-region average per month of the total number of the observed DCCs and are calculated depending on the extension of each sub-region. There is a clear dominance of the Transition sub-region with the highest values (and with the highest variability as well) of observed DCC frequencies throughout almost the entire annual cycle. In this sub-region, two key elements are present: the moisture advection from both the Gulf of Mexico and the Pacific Ocean and the mountainous areas located over the TMVB and the Sierras Madres, enabling orographic convection. Such elements seem to modulate the high frequency of DCCs, mainly over the highest elevations. In the Neotropical sub-region, the presence of a sea breeze over the coastal plains with large mountainous areas perpendicular to the fluxes spread is considered to be the main element in the second-highest observed DCC frequencies. The peak shown in September in this sub-region is related to the passage of tropical cyclones (Figure 8a), and the generation of stratiform clouds (by sea breeze effect) is the cause of the high values of CF (Figure 8b). The Nearctic sub-region holds the minimum frequency of DCCs and the lowest values of CF. This part of Mexico is characterized as the southernmost zone of the dry portion of the country (Chihuahua Desert) [62]. In general terms, in the Transition sub-region, all the necessary key elements for deep convection activity converge, in the Neotropical sub-region, here is a significant influence of sea breeze and the pass of tropical cyclones, while the Nearctic sub-region holds the dryer characteristics.

A decrease in frequency is detected in August for both CF and DCC. Such behavior has been identified in all the sub-regions, but is most evident in the Transition sub-region. This period can be related to the midsummer drought—i.e., *canícula*—in Mexico. Such a signal of the midsummer drought was also observed in a daily precipitation dataset based on a combination of station and satellite data for Mexico [63]. However, an in-depth and more detailed analysis of the midsummer drought event and how it relates to our observations is necessary for future studies. To the best of our knowledge, the identification of a drought marker in the summertime, the “*canícula*”, in the deep convective cloud frequencies obtained from satellite measurements (in this case MODIS) in this part of the country is new.

Similar behaviors can be observed in the precipitation values obtained from the CHIRPS dataset (Figure 8c,d). In the threshold values for the 90th percentile, the Neotropical sub-region holds both higher values and variability. The peak of September is again related to the passage of tropical cyclones. On the other hand, the Nearctic sub-region holds the lowest frequencies and variability, which means relatively steady dry environments. The Transition zone shows intermediate variability. As with the MODIS cloud observations, a clear decrease in August is present. The number of days with precipitation exceeding 10 mm shows the similarities between the Neotropical and the Transition sub-regions. Although these values are consistently higher in the Neotropical sub-region, the curves show a high correlation (Figure 8d). The variability shown in the Neotropical and Transition sub-regions is related to dynamic processes (as moisture fluxes) and static features (as the complex terrain). The patterns shown here prove the significant influence of the Pacific Ocean and the Gulf of Mexico in the modulation of deep convective clouds and precipitation regimes over the central parts of the country. Finally, the minimum value between two maximums values (i.e. the *canícula* signature) in the Nearctic sub-region is less clear than in the previous analysis.

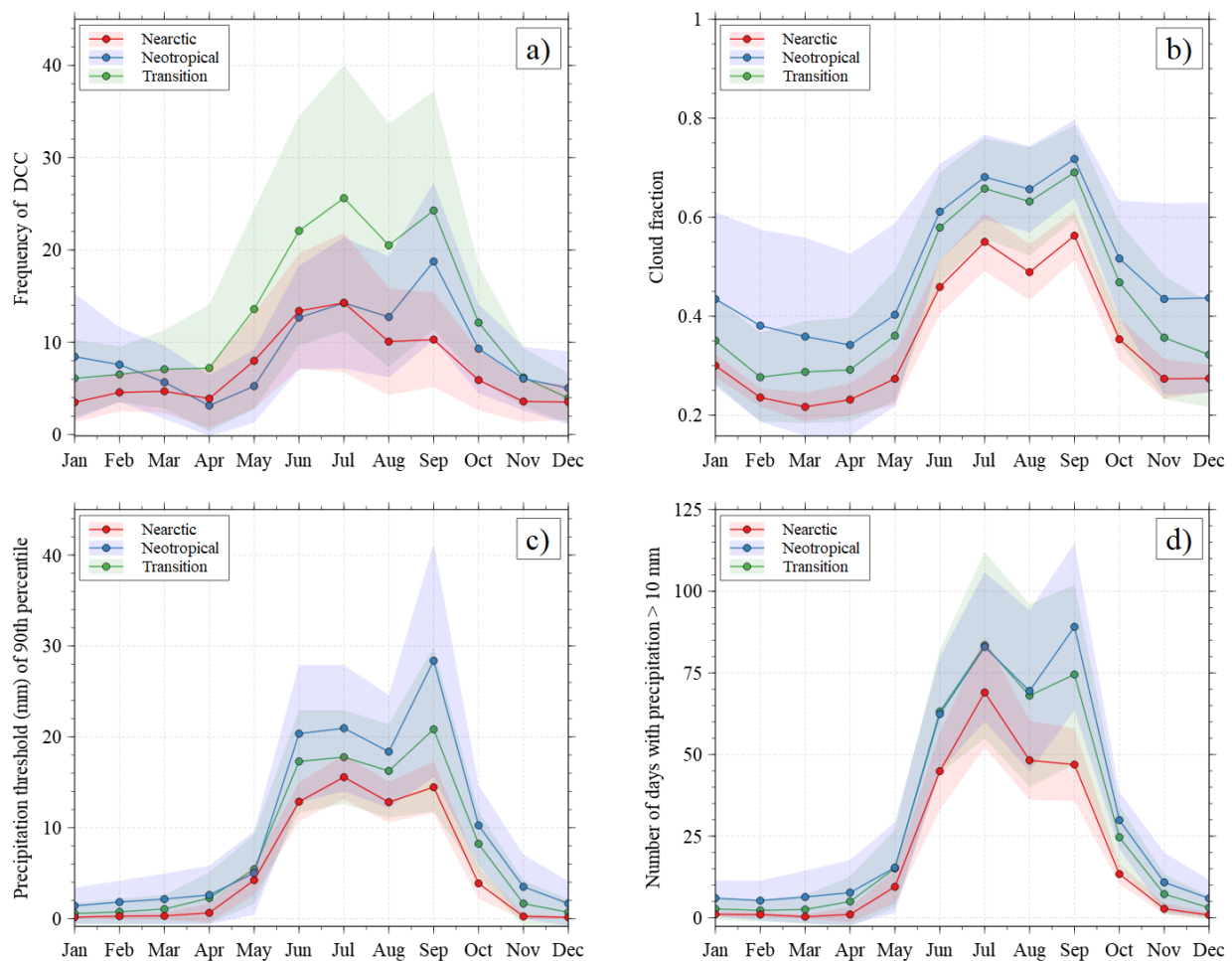


Figure 8. Monthly means (lines) and one standard deviation (shaded areas) of (a) observed deep convective cloud (DCC) frequency, (b) cloud fraction (CF), (c) precipitation threshold values and (d) number of days with precipitation exceeding 10 mm per Nearctic, Neotropical, and Transition sub-regions.

4.5. Inter-Annual Variability

Changes in wind regimens, climatic oscillations and tropical cyclone activity can play a significant role in the spatio-temporal distribution of precipitation [64,65]. In the study area, where convective precipitation is relevant, research to improve the understanding of the reasons behind spatio-temporal variations of deep convective activity, also on larger temporal scales, can further benefit from estimates of inter-annual variabilities of deep convective cloud frequencies obtained from satellite observations. To this end, the annual anomaly of the total number of observed DCC is presented for the 10 year time period; see Figure 9. The annual DCC anomaly results from the difference between the annual mean (2008–2017) and the value of the year of analysis. From this, the presence of relatively dry (e.g., 2011, 2017) and wet (2010, 2013, 2015) years can be identified within this 10 year time period. The transition between wet or dry years can be divided into an explosive stage—i.e., the change comes from one year to another; for example, 2010–2011—or a progressive stage, where the change comes with an intermediate year; for example, 2011–2012–2013. Interestingly, the transitions identified through the anomalies in Figure 9 are more distinct over the coastal regions, at the east and west edges of the domain, suggesting that these regions are more sensitive to large-scale dynamic changes. It is important to mention that the increase or decrease of observed DCC frequency can be concentrated in only a couple of months within the 10 year time period. For example, from Figure 8a it is evident that the Transition sub-region shows a significant variability mainly in the summer months.

Moreover, for the coastal regions, especially in the east, the annual mean DCC frequency difference between two subsequent years (2010 and 2011) can be about twice as large as the largest difference between monthly means inferable from Figure 8a (Neotropical sub-region), indicating the relevant impact of (changes in) large-scale dynamics on observed annual DCC distribution in the study area.

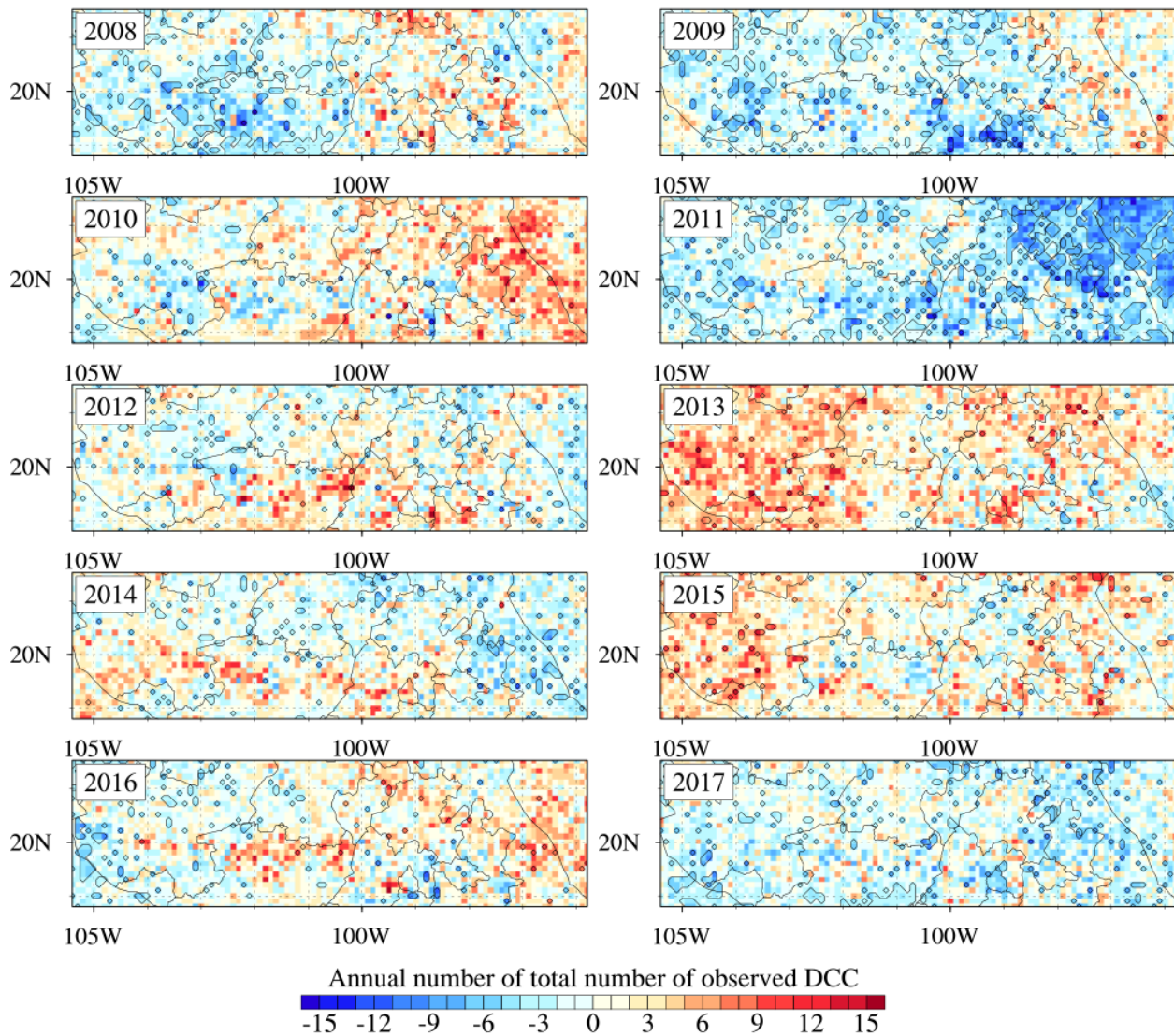


Figure 9. Annual anomaly of the total number of observed deep convective clouds (2008–2017) based on MODIS cloud data, with a horizontal resolution of 0.1 degrees. The black lines indicate the grid boxes with a significant anomaly.

A one-sample, two-sided student t-test was performed to identify where external events (such as climatic oscillations) could be mainly responsible for the modification of the annual statistical values of the number of convective events in the Trans-Mexican Volcanic Belt and where local events predominate. The hypothesis was applied that the mean value of the number of convective events of a specific year did not vary significantly concerning the mean value of the data set of the entire 10 year period considered. Figure 9 includes the results for the period 2008–2017 for a confidence level of 95%. In the year 2011, it is observed that there is a large region in the northeast where the hypothesis is rejected. This indicates that external processes might influence and modify the number of convective events. There are other small regions, predominantly in the southern part, where the hypothesis is also rejected. Changes in weather regimes derived from the influence of climatic oscillations could have an impact on the study area and the DCC frequency. These preliminary findings

indicate the necessity to perform more in-depth analyses on observational datasets that extend beyond 10 years to further investigate which dynamics cause these modifications. Furthermore, climatic oscillations (e.g., the Madden–Julian Oscillation (MJO), El Niño Southern Oscillation (ENSO) and the Pacific Decadal Oscillation (PDO)) must be taken into account in the study of processes that might influence the generation and observed frequency of DCC.

5. Conclusions

The Trans-Mexican Volcanic Belt is a complex orography zone in central Mexico in which a large number of manifestations of severe weather has been documented. This area concentrates a large population exposed to severe weather events such as tornadoes and heavy precipitation with accompanying flash floods, making the improved forecasting, detection and monitoring of deep convective cloud systems and associated severe weather of great importance. Due to the lack of a dense ground-based observational network for the extensive detection and monitoring of severe weather phenomena in the country, satellite observations of cloud and precipitation events provide a suitable and affordable alternative to characterize and improve our understanding of deep convective events in Mexico.

This work contributes to an improved understanding of the occurrence and natural variability of deep convective events in the TMVB region by performing a first estimation and assessment of satellite-observed spatio-temporal distribution of deep convective clouds using well-established MODIS cloud products. The study area exhibits large variations in elevations, including mountainous areas with heights of up to 5000 m along the TMVB. It serves as a transition zone between a drier (north) and more humid (south) climate, leading to a large variety of land surface characteristics [33], and is known to be subject to the differential influence of the Gulf of Mexico (east) and the Pacific Ocean (west) [58,66] with corresponding moisture fluxes and large-scale dynamics [67]. The substantial climatic and environmental regional differences within the study area allow, by studying geographical variations, first indications of the impact of local conditions, such as terrain features, to be considered, as well as the impacts of large-scale conditions on the observed distinct spatio-temporal variabilities of DCCs.

Monthly climatology data for 10 years (2008 to 2017) of the cloud fraction and the frequency of deep convective clouds along the TMVB in Mexico on a 0.1 degree resolution have been produced using a combination of MODIS Coll. 6 cloud products. The analysis of 10 years of satellite observations shows the clear establishment of wet and dry phases characterized by cloud abundance, and more specifically, deep convective cloud frequency, preceded by transition phases. The first peak observed in the deep convective cloud frequency in July can be related to the change in the wind patterns that increase the moisture advection from both the Pacific Ocean and the Gulf of Mexico [66,68]. The second observed DCC frequency peak in September is related to the frequent passage of easterly waves and tropical cyclones during that time of year [60]. The spatial variability within the study area is greatest for the summertime period, though large, persistent cloud fields can be found in the eastern part throughout the entire year.

The spatio-temporal patterns of deep convective cloud frequency have been related to extreme weather events; i.e., extreme rain episodes obtained from precipitation data from the CHIRPS in-situ and satellite-based dataset. A very similar pattern of the spatio-temporal distribution of extreme precipitation days and deep convective clouds was found. For both, the highest frequencies align just over the higher elevations of the TMVB, indicating the important role of orography in the development of convective systems. Calculations of the 90th percentile of precipitation show extremely high variations in a relatively small geographical area. Again, higher values are related to the higher regions with a complex orography.

For domain-averaged seasonal patterns, a strong correlation was found between observed DCC frequency and precipitation (with a correlation coefficient of 0.84). The frequencies of the DCCs and precipitation events show a clear decrease in August, which

corresponds well with the description of the midsummer drought phenomena in Mexico—the so-called “canícula”—provided by others [49,63]. To our knowledge, the midsummer drought is observed and documented for the first time using satellite-observed deep convective cloud frequencies as an identification marker in the region. Whereas the first peak in the DDC frequency and precipitation can be associated with the moisture advection from the oceans [66,68], the second peak observed in September might be affected by the increase in tropical cyclone activity [60], as mentioned before.

Another relevant outcome is the solid relationship between the terrain configuration and the observed DCC frequency with the higher correlation coefficient of 0.77 computed along a cross-section with the highest elevations. The complex terrain of the TMVB seems to be essential for the generation of deep convective clouds by forced convection and significantly controls the satellite-observed DCC and extreme precipitation frequencies. Similar results have been reported before in central Mexico using model simulations [69]. Moreover, observations from one radar site covering Mexico city show a similar behavior [27]. Due to their geographical position, the mountains of the TMVB, located in central Mexico, have a direct influence on wet air masses from both the Pacific Ocean and the Gulf of Mexico [66,70] and dry air masses related to the cold fronts propagated from the north [31,61]. This is also reinforced by the analysis from the sub-region perspective, which provides a first insight into the relative impact of different local and large-scale conditions and accompanying physical processes that lead to the observed spatio-temporal variability of deep convective clouds and associated severe weather. The high cloudiness over all of the Gulf of Mexico allows the identification of the possibly important role of sea breeze [52] and the position of the mountains (perpendicular to moisture advection) for the eastern portion of the Neotropical sub-region. Cold fronts and Föhn effects [34,55] influence the Nearctic sub-region; i.e., drylands in the north portion of the domain. The analysis of the behavior of convective events allowed the identification of similarities across the Transition sub-region. This relation is associated with the influence of moisture advection processes from the Pacific Ocean and the Gulf of Mexico [66]. The greatest observed DCC frequency in this sub-region seems to be a result of complex interactions between terrain, moisture fluxes and relatively cold air masses from the north.

Finally, the analysis of the inter-annual variability of observed deep convective clouds shows years with clearly positive and negative anomalies, though both the variability within the domain for one year and the domain-averaged variability within one year can be as large as between years. A future study regarding this topic will benefit from a temporal extension of the observational datasets. Even though the development of deep convection here seems to have a strong regional component (i.e., terrain configuration), the moisture availability for their initiation is related to changes in wind patterns. Changes in the weather patterns can be associated with the El Niño Southern Oscillation, the Pacific Decadal Oscillation or the Madden–Julian Oscillation [64,71–73]. In this sense, a larger dataset is required to investigate the relative impact of these climatic oscillations on DCC frequency, and future work should be focused on this topic as well.

Considering that the independent types of observational datasets used in this study show a clear relationship, this represent an encouragement to continue and extend these kinds of satellite-based studies on deep convective clouds and associated severe weather, especially in situations with an absence of large-scale radar coverage, as is the case for Mexico. In that sense, this study contributes considerably to a first characterization of the environment in which extreme weather phenomena occur. Furthermore, the study brings to light the possibility of identifying and quantifying region-specific climatological characteristics, such as the “canícula”, with the use of satellite observations of clouds and precipitation. Knowing that a wide range of dynamical processes controls the formation of deep convective cloud systems and the accompanying variability in characteristics, observational-based approaches can obviously benefit from reinforcement through in-depth studies including extensive numerical weather simulations. In turn, satellite-observed distributions of clouds and precipitation can provide modelers with valuable information about the quality of

parameterizations related to convective processes in large-scale models. While the straightforward CTP–COT threshold-based DCC cloud typing method used in this study can provide a first estimate of the frequency of clouds with considerable vertical extent and liquid/ice content, more sophisticated cloud classification schemes should be considered in future studies. For example, k-means clustering methods might provide (deep convective) cloud regimes that are tuned to the particular meteorological/climatological conditions in a study area.

Several satellite-based observations can be added to further improve our understanding as well as the monitoring of deep convective processes in Mexico. For example, cloud observations obtained from advanced imagers, with relatively high spatial resolution and high temporal coverage of minutes, mounted on the NOAA Geostationary Operational Environmental Satellite (GOES)-R series [74,75], can be used to investigate the diurnal cycle of convective clouds in Mexico. Furthermore, satellite observations of, e.g., water vapor and surface temperature, can be used to characterize and study the conditions in the pre-convective and convective initiation environment.

Supplementary Materials: The following are available at <https://www.mdpi.com/2072-4292/13/6/1215/s1>. Figure S1: Spatial distribution of temporal correlation computed for MODIS (frequency of deep, convective clouds) and CHIRPS (accumulated precipitation) for four seasons (December–February DJF; March–May MAM; June–August JJA; September–November SON). Highest correlation values are found for SON (domain-average 0.93), especially over larger terrain elevations. For JJA (domain-average 0.81), the correlation values vary much more within the study area, which can at least partly be explained by the generally very high observed variability (std) of DCC frequency for those months (also seen in Figure 8 in the manuscript). For DJF (domain-average 0.79) and MAM (domain-average 0.77), the spatial distribution looks smoother again. Here, DCC frequency and precipitation amounts are generally much lower as well as the variability. However, for MAM, with already increased DCC frequencies in May, higher correlation values can be clearly observed along the TMVB. The maps are added as supplementary material including a short description.

Author Contributions: Conceptualization, N.C., J.F.L.-C., C.C.H.; methodology, J.F.L.-C., C.C.H., N.C.; software, J.F.L.-C.; validation, J.F.L.-C., C.C.H., N.C.; formal analysis, J.F.L.-C., C.C.H., N.C.; investigation, J.F.L.-C., C.C.H., N.C.; resources, N.C., J.F.L.-C., C.C.H.; data curation, J.F.L.-C., C.C.H.; writing—original draft preparation, J.F.L.-C., C.C.H., N.C.; writing—review and editing, J.F.L.-C., C.C.H., N.C., J.F.; visualization, J.F.L.-C.; supervision, N.C., J.F.; project administration, N.C., J.F.; funding acquisition, N.C., J.F. All authors have read and agreed to the published version of the manuscript.

Funding: This research was funded by the Consejo Nacional de Ciencia y Tecnología (CONACYT)—Mexico (Grant Number 298737) and by the Deutsche Forschungsgemeinschaft (DFG, German Research Foundation)-FOR 2589. The publication of this article was funded by Freie Universität Berlin.

Data Availability Statement: Publicly available datasets were analyzed in this study. The processed data can be found here: ftp://jericho.met.fu-berlin.de/pub/data_remotesensing-1117127, accessed on 22 March 2021.

Acknowledgments: We are very grateful to the two anonymous reviewers for their constructive comments.

Conflicts of Interest: The authors declare no conflict of interest.

Abbreviations

The following abbreviations are used in this manuscript:

AVHRR	Advanced Very-High Resolution Radiometer
CHIRPS	Climate Hazards Group Infrared Precipitation with Station data
CF	Cloud fraction
COT	Cloud optical thicknesses
CTP	Cloud top pressure
DCC	Deep convective cloud
GOES	Geostationary Operational Environmental Satellite
ISCCP	International Satellite Cloud Climatology Project

MCS	Mesoscale convective systems
MODIS	Moderate Resolution Imaging Spectroradiometer
TMVB	Trans-Mexican Volcanic Belt

Appendix A

Land cover legend (INEGI-USGS) for Figure 1d.

1	Urban and built-up land
2	Dryland cropland and pasture
3	Irrigated cropland and pasture
4	Mixed dryland/irrigated cropland and pasture
5	Cropland/grassland mosaic
6	Cropland/woodland mosaic
7	Grassland
8	Shrubland
9	Mixed shrubland/grassland
10	Savanna
11	Deciduous broadleaf forest
12	Deciduous needleleaf forest
13	Evergreen broadleaf forest
14	Evergreen needleleaf forest
15	Mixed forest
16	Water bodies
17	Herbaceous wetland
18	Wooded wetland
19	Barren or sparsely vegetated
20	Herbaceous tundra
21	Wooded tundra
22	Mixed tundra
23	Bare ground tundra
24	Snow or ice
100	Unclassified

References

- Bony, S.; Stevens, B.; Frierson, D.M.; Jakob, C.; Kageyama, M.; Pincus, R.; Shepherd, T.G.; Sherwood, S.C.; Siebesma, A.P.; Sobel, A.H.; et al. Clouds, circulation and climate sensitivity. *Nat. Geosci.* **2015**, *8*, 261. [[CrossRef](#)]
- Stephens, G.L. Cloud feedbacks in the climate system: A critical review. *J. Clim.* **2005**, *18*, 237–273. [[CrossRef](#)]
- Fu, Q.; Yang, P.; Sun, W. An accurate parameterization of the infrared radiative properties of cirrus clouds for climate models. *J. Clim.* **1998**, *11*, 2223–2237. [[CrossRef](#)]
- Tselioudis, G.; Jakob, C. Evaluation of midlatitude cloud properties in a weather and a climate model: Dependence on dynamic regime and spatial resolution. *J. Geophys. Res. Atmos.* **2002**, *107*, AAC-14. [[CrossRef](#)]
- King, M.D.; Platnick, S.; Menzel, W.P.; Ackerman, S.A.; Hubanks, P.A. Spatial and temporal distribution of clouds observed by MODIS onboard the Terra and Aqua satellites. *IEEE Trans. Geosci. Remote Sens.* **2013**, *51*, 3826–3852. [[CrossRef](#)]
- Tan, J.; Jakob, C.; Rossow, W.B.; Tselioudis, G. Increases in tropical rainfall driven by changes in frequency of organized deep convection. *Nature* **2015**, *519*, 451–454. [[CrossRef](#)] [[PubMed](#)]
- Hoeppe, P. Trends in weather related disasters—Consequences for insurers and society. *Weather Clim. Extrem.* **2016**, *11*, 70–79. [[CrossRef](#)]
- Groenemeijer, P.; Púčik, T.; Holzer, A.M.; Antonescu, B.; Riemann-Campe, K.; Schultz, D.M.; Kühne, T.; Feuerstein, B.; Brooks, H.E.; Doswell, C.A., III; et al. Severe convective storms in Europe: Ten years of research and education at the European severe storms laboratory. *Bull. Am. Meteorol. Soc.* **2017**, *98*, 2641–2651. [[CrossRef](#)]
- Alcántara-Ayala, I. Disasters in Mexico and Central America: A little bit more than a century of natural hazards. *Dev. Earth Surf. Process.* **2009**, *13*, 75–97.
- Yano, J.I.; Ziemiański, M.Z.; Cullen, M.; Termonia, P.; Onvlee, J.; Bengtsson, L.; Carrassi, A.; Davy, R.; Deluca, A.; Gray, S.L.; et al. Scientific challenges of convective-scale numerical weather prediction. *Bull. Am. Meteorol. Soc.* **2018**, *99*, 699–710. [[CrossRef](#)]
- Sun, J.; Xue, M.; Wilson, J.W.; Zawadzki, I.; Ballard, S.P.; Onvlee-Hoimeyer, J.; Joe, P.; Barker, D.M.; Li, P.W.; Golding, B.; et al. Use of NWP for nowcasting convective precipitation: Recent progress and challenges. *Bull. Am. Meteorol. Soc.* **2014**, *95*, 409–426. [[CrossRef](#)]

12. Martius, O.; Hering, A.; Kunz, M.; Manzato, A.; Mohr, S.; Nisi, L.; Trefalt, S. Challenges and Recent Advances in Hail Research. *Bull. Am. Meteorol. Soc.* **2018**, *99*, ES51–ES54. [[CrossRef](#)]
13. Johnson, R.H.; Mapes, B.E. Mesoscale processes and severe convective weather. In *Severe Convective Storms*; Springer: Berlin, Germany, 2001; pp. 71–122.
14. Serafin, S.; Adler, B.; Cuxart, J.; De Wekker, S.F.; Gohm, A.; Grisogono, B.; Kalthoff, N.; Kirshbaum, D.J.; Rotach, M.W.; Schmidli, J.; et al. Exchange processes in the atmospheric boundary layer over mountainous terrain. *Atmosphere* **2018**, *9*, 102. [[CrossRef](#)]
15. Doswell, C.A., III; Brooks, H.E.; Maddox, R.A. Flash flood forecasting: An ingredients-based methodology. *Weather. Forecast.* **1996**, *11*, 560–581. [[CrossRef](#)]
16. Brooks, H.E.; Lee, J.W.; Craven, J.P. The spatial distribution of severe thunderstorm and tornado environments from global reanalysis data. *Atmos. Res.* **2003**, *67*, 73–94. [[CrossRef](#)]
17. Taszarek, M.; Brooks, H.E.; Czernecki, B.; Szuster, P.; Fortuniak, K. Climatological aspects of convective parameters over Europe: A comparison of ERA-interim and sounding data. *J. Clim.* **2018**, *31*, 4281–4308. [[CrossRef](#)]
18. Matsudo, C.; Salio, P.V. Severe weather reports and proximity to deep convection over Northern Argentina. *Atmos. Res.* **2011**, *100*, 523–537. [[CrossRef](#)]
19. Goudenhoofdt, E.; Delobbe, L. Statistical characteristics of convective storms in Belgium derived from volumetric weather radar observations. *J. Appl. Meteorol. Climatol.* **2013**, *52*, 918–934. [[CrossRef](#)]
20. Devasthale, A.; Fueglistaler, S. A climatological perspective of deep convection penetrating the TTL during the Indian summer monsoon from the AVHRR and MODIS instruments. *Atmos. Chem. Phys.* **2010**, *10*, 4573–4582. [[CrossRef](#)]
21. Takahashi, H.; Luo, Z.J. Characterizing tropical overshooting deep convection from joint analysis of CloudSat and geostationary satellite observations. *J. Geophys. Res. Atmos.* **2014**, *119*, 112–121. [[CrossRef](#)]
22. Carbajal Henken, C.; Schmeits, M.J.; Deneke, H.; Roebeling, R.A. Using MSG-SEVIRI cloud physical properties and weather radar observations for the detection of Cb/TCu clouds. *J. Appl. Meteorol. Climatol.* **2011**, *50*, 1587–1600. [[CrossRef](#)]
23. Rosenfeld, D.; Woodley, W.L.; Lerner, A.; Kelman, G.; Lindsey, D.T. Satellite detection of severe convective storms by their retrieved vertical profiles of cloud particle effective radius and thermodynamic phase. *J. Geophys. Res. Atmos.* **2008**, *113*. [[CrossRef](#)]
24. Valdés-Manzanilla, A. Mesoscale convective systems in NW Mexico during the strong ENSO events of 1997–1999. *Atmósfera* **2015**, *28*, 143–148. [[CrossRef](#)]
25. Zúñiga, E.; Magaña, V. Vulnerability and risk to intense rainfall in Mexico: The effect of land use cover change. *Investig. Geogr.* **2018**, *95*, 1–18.
26. Kucieńska, B.; Raga, G.; Rodríguez, O. Cloud-to-ground lightning over Mexico and adjacent oceanic regions: A preliminary climatology using the WWLLN dataset. In *Annales Geophysicae*; Copernicus GmbH: Antalya, Turkey, 2010; Volume 28, pp. 2047–2057.
27. Novo, S.; Raga, G.B. The properties of convective storms in central Mexico: A radar and lightning approach. *Atmósfera* **2013**, *26*, 461–472. [[CrossRef](#)]
28. Edwards, R. Supercells of the Serranías del Burro (Mexico). In Proceedings of the 23rd Conference on Severe Local Storms, St. Louis, MO, USA, 6–10 November 2006.
29. León-Cruz, J.F.; Carbajal, N.; Pineda-Martínez, L.F. Meteorological analysis of the tornado in Ciudad Acuña, Coahuila State, Mexico, on May 25, 2015. *Nat. Hazards* **2017**, *89*, 423–439. [[CrossRef](#)]
30. León-Cruz, J.F.; Carbajal, N.; Pineda-Martínez, L. The role of complex terrain in the generation of tornadoes in the west of Mexico. *Nat. Hazards* **2019**, *97*, 1–19. [[CrossRef](#)]
31. Carbajal, N.; León-Cruz, J.F.; Pineda-Martínez, L.F.; Tuxpan-Vargas, J.; Gaviño-Rodríguez, J.H. Occurrence of Anticyclonic Tornadoes in a Topographically Complex Region of Mexico. *Adv. Meteorol.* **2019**, *2019*, 1–11. [[CrossRef](#)]
32. León-Cruz, J.F. Climatología y Meteorología de Tornados en México. Ph.D. Thesis, Instituto Potosino de Investigación Científica y Tecnológica, A.C., San Luis Potosí, Mexico, 2019.
33. Morrone, J.J.; Escalante, T.; Rodríguez-Tapia, G. Mexican biogeographic provinces: Map and shapefiles. *Zootaxa* **2017**, *4277*, 277–279. [[CrossRef](#)]
34. Abatzoglou, J.T.; Hatchett, B.J.; Fox-Hughes, P.; Gershunov, A.; Nauslar, N.J. Global Climatology of Synoptically-Forced Downslope Winds. *Int. J. Climatol.* **2020**, *41*, 31–50. [[CrossRef](#)]
35. Platnick, S.; Ackerman, S.; King, M.; Meyer, K.; Menzel, W.; Holz, R.; Baum, B.; Yang, P. MODIS atmosphere L2 cloud product (06_L2). *NASA MODIS Adapt. Process. Syst. Goddard Space Flight Cent.* **2015**, *10*, 1–53.
36. Platnick, S.; Meyer, K.G.; King, M.D.; Wind, G.; Amarasinghe, N.; Marchant, B.; Arnold, G.T.; Zhang, Z.; Hubanks, P.A.; Holz, R.E.; et al. The MODIS cloud optical and microphysical products: Collection 6 updates and examples from Terra and Aqua. *IEEE Trans. Geosci. Remote Sens.* **2016**, *55*, 502–525. [[CrossRef](#)]
37. Platnick, S.; King, M.D.; Ackerman, S.A.; Menzel, W.P.; Baum, B.A.; Riédi, J.C.; Frey, R.A. The MODIS cloud products: Algorithms and examples from Terra. *IEEE Trans. Geosci. Remote Sens.* **2003**, *41*, 459–473. [[CrossRef](#)]
38. Yuan, T.; Li, Z. General macro-and microphysical properties of deep convective clouds as observed by MODIS. *J. Clim.* **2010**, *23*, 3457–3473. [[CrossRef](#)]
39. Jin, D.; Oreopoulos, L.; Lee, D.; Tan, J.; Kim, K.M. Large-Scale Characteristics of Tropical Convective Systems Through the Prism of Cloud Regime. *J. Geophys. Res. Atmos.* **2020**, *125*, e2019JD031157. [[CrossRef](#)] [[PubMed](#)]

40. Ntwali, D.; Chen, H. Diurnal spatial distributions of aerosol optical and cloud micro-macrophysics properties in Africa based on MODIS observations. *Atmos. Environ.* **2018**, *182*, 252–262. [[CrossRef](#)]
41. Rossow, W.B.; Schiffer, R.A. Advances in understanding clouds from ISCCP. *Bull. Am. Meteorol. Soc.* **1999**, *80*, 2261–2288. [[CrossRef](#)]
42. Young, A.H.; Bates, J.J.; Curry, J.A. Application of cloud vertical structure from CloudSat to investigate MODIS-derived cloud properties of cirriform, anvil, and deep convective clouds. *J. Geophys. Res. Atmos.* **2013**, *118*, 4689–4699. [[CrossRef](#)]
43. Price, C. Global thunderstorm activity. In *Sprites, Elves and Intense Lightning Discharges*; Springer: Berlin, Germany, 2006; pp. 85–99.
44. Funk, C.; Peterson, P.; Landsfeld, M.; Pedreros, D.; Verdin, J.; Shukla, S.; Husak, G.; Rowland, J.; Harrison, L.; Hoell, A.; et al. The climate hazards infrared precipitation with stations—a new environmental record for monitoring extremes. *Sci. Data* **2015**, *2*, 150066. [[CrossRef](#)]
45. Katsanos, D.; Retalis, A.; Michaelides, S. Validation of a high-resolution precipitation database (CHIRPS) over Cyprus for a 30-year period. *Atmos. Res.* **2016**, *169*, 459–464. [[CrossRef](#)]
46. Katsanos, D.; Retalis, A.; Tymvios, F.; Michaelides, S. Analysis of precipitation extremes based on satellite (CHIRPS) and in situ dataset over Cyprus. *Nat. Hazards* **2016**, *83*, 53–63. [[CrossRef](#)]
47. Paredes-Trejo, F.J.; Barbosa, H.; Kumar, T.L. Validating CHIRPS-based satellite precipitation estimates in Northeast Brazil. *J. Arid. Environ.* **2017**, *139*, 26–40. [[CrossRef](#)]
48. Martínez-Lopez, B.; Quintanar, A.; Cabos-Narvaez, W.; Gay-García, C.; Sein, D. Nonlinear trends and nonstationary oscillations as extracted from annual accumulated precipitation at Mexico City. *Earth Space Sci.* **2018**, *5*, 473–485. [[CrossRef](#)]
49. Perdigón-Morales, J.; Romero-Centeno, R.; Pérez, P.O.; Barrett, B.S. The midsummer drought in Mexico: Perspectives on duration and intensity from the CHIRPS precipitation database. *Int. J. Climatol.* **2018**, *38*, 2174–2186. [[CrossRef](#)]
50. Climate Hazards Center. *CHIRPS: Rainfall Estimates from Rain Gauge and Satellite Observations*; Climate Hazards Center: Santa Barbara, CA, USA, 2015.
51. Ochoa, C.A.; Quintanar, A.I.; Raga, G.B.; Baumgardner, D. Changes in intense precipitation events in Mexico City. *J. Hydrometeorol.* **2015**, *16*, 1804–1820. [[CrossRef](#)]
52. Pérez-Méndez, M.; Tejada-Martínez, A.; Fitzjarrald, D.R. Diurnal Variation of Rainfall in a Tropical Coastal Region with Complex Orography. *Atmosphere* **2019**, *10*, 604. [[CrossRef](#)]
53. Miller, S.; Keim, B.; Talbot, R.; Mao, H. Sea breeze: Structure, forecasting, and impacts. *Rev. Geophys.* **2003**, *41*. [[CrossRef](#)]
54. Passalacqua, G.; Sheinbaum, J.; Martínez, J. Sea surface temperature influence on a winter cold front position and propagation: Air–sea interactions of the ‘Nortes’ winds in the Gulf of Mexico. *Atmos. Sci. Lett.* **2016**, *17*, 302–307. [[CrossRef](#)]
55. Luna-Niño, R.; Cavazos, T. Formation of a coastal barrier jet in the Gulf of Mexico due to the interaction of cold fronts with the Sierra Madre Oriental mountain range. *Q. J. R. Meteorol. Soc.* **2018**, *144*, 115–128. [[CrossRef](#)]
56. Cavazos, T.; Hastenrath, S. Convection and rainfall over Mexico and their modulation by the Southern Oscillation. *Int. J. Climatol.* **1990**, *10*, 377–386. [[CrossRef](#)]
57. Pineda-Martínez, L.F.; Carbajal, N.; Campos-Ramos, A.A.; Noyola-Medrano, C.; Aragón-Piña, A. Numerical research of extreme wind-induced dust transport in a semi-arid human-impacted region of Mexico. *Atmos. Environ.* **2011**, *45*, 4652–4660. [[CrossRef](#)]
58. Giovannetone, J.P.; Barros, A.P. A remote sensing survey of the role of landform on the organization of orographic precipitation in central and southern Mexico. *J. Hydrometeorol.* **2008**, *9*, 1267–1283. [[CrossRef](#)]
59. Knapp, K.R.; Kruk, M.C.; Levinson, D.H.; Diamond, H.J.; Neumann, C.J. The international best track archive for climate stewardship (IBTrACS) unifying tropical cyclone data. *Bull. Am. Meteorol. Soc.* **2010**, *91*, 363–376. [[CrossRef](#)]
60. Jáuregui, E. Climatology of landfalling hurricanes and tropical storms in Mexico. *Atmósfera* **2003**, *16*, 193–204.
61. Pineda-Martínez, L.F.; Carbajal, N. Mesoscale numerical modeling of meteorological events in a strong topographic gradient in the northeastern part of Mexico. *Clim. Dyn.* **2009**, *33*, 297–312. [[CrossRef](#)]
62. Pineda-Martínez, L.F.; Carbajal, N. Climatic analysis linked to land vegetation cover of Mexico by applying multivariate statistical and clustering analysis. *Atmósfera* **2017**, *30*, 233–242. [[CrossRef](#)]
63. Magaña, V.; Amador, J.A.; Medina, S. The midsummer drought over Mexico and Central America. *J. Clim.* **1999**, *12*, 1577–1588. [[CrossRef](#)]
64. Magaña, V.; Vázquez, J.L.; Pérez, J.L.; Pérez, J.B. Impact of El Niño on precipitation in Mexico. *Geofísica Int.* **2003**, *42*, 313–330.
65. Breña-Naranjo, J.A.; Pedrozo-Acuña, A.; Pozos-Estrada, O.; Jiménez-López, S.A.; López-López, M.R. The contribution of tropical cyclones to rainfall in Mexico. *Phys. Chem. Earth Parts A/B/C* **2015**, *83*, 111–122. [[CrossRef](#)]
66. Mo, K.C.; Chelliah, M.; Carrera, M.L.; Higgins, R.W.; Ebisuzaki, W. Atmospheric moisture transport over the United States and Mexico as evaluated in the NCEP regional reanalysis. *J. Hydrometeorol.* **2005**, *6*, 710–728. [[CrossRef](#)]
67. Gimeno, L.; Dominguez, F.; Nieto, R.; Trigo, R.; Drumond, A.; Reason, C.J.; Taschetto, A.S.; Ramos, A.M.; Kumar, R.; Marengo, J. Major mechanisms of atmospheric moisture transport and their role in extreme precipitation events. *Annu. Rev. Environ. Resour.* **2016**, *41*, 117–141. [[CrossRef](#)]
68. Serra, Y.L.; Kiladis, G.N.; Hodges, K.I. Tracking and mean structure of easterly waves over the Intra-Americas Sea. *J. Clim.* **2010**, *23*, 4823–4840. [[CrossRef](#)]
69. Bhushan, S.; Barros, A. A numerical study to investigate the relationship between moisture convergence patterns and orography in central Mexico. *J. Hydrometeorol.* **2007**, *8*, 1264–1284. [[CrossRef](#)]

70. Xu, H.; Xie, S.P.; Wang, Y.; Small, R.J. Effects of Central American mountains on the eastern Pacific winter ITCZ and moisture transport. *J. Clim.* **2005**, *18*, 3856–3873. [[CrossRef](#)]
71. Pavia, E.G.; Graef, F.; Reyes, J. PDO–ENSO effects in the climate of Mexico. *J. Clim.* **2006**, *19*, 6433–6438. [[CrossRef](#)]
72. Barlow, M.; Salstein, D. Summertime influence of the Madden-Julian Oscillation on daily rainfall over Mexico and Central America. *Geophys. Res. Lett.* **2006**, *33*. [[CrossRef](#)]
73. Bravo-Cabrera, J.L.; Azpra-Romero, E.; Zarraluqui-Such, V.; Gay-García, C. Effects of El Niño in Mexico during rainy and dry seasons: An extended treatment. *Atmósfera* **2017**, *30*, 221–232. [[CrossRef](#)]
74. Schmit, T.J.; Gunshor, M.M.; Menzel, W.P.; Gurka, J.J.; Li, J.; Bachmeier, A.S. Introducing the next-generation Advanced Baseline Imager on GOES-R. *Bull. Am. Meteorol. Soc.* **2005**, *86*, 1079–1096. [[CrossRef](#)]
75. Schmit, T.J.; Griffith, P.; Gunshor, M.M.; Daniels, J.M.; Goodman, S.J.; Lebar, W.J. A closer look at the ABI on the GOES-R series. *Bull. Am. Meteorol. Soc.* **2017**, *98*, 681–698. [[CrossRef](#)]